Programmable structure with shape memory materials for soft robotics

IOP Publishing Smart Mater. Struct. 35 (2026) 015049 https://doi.org/10.1088/1361-665X/ae2a85

Smart Materials and Structures

PAPER

Programmable structure with shape memory materials for soft robotics

Qianyi Chen*[,1], Ruochen Wu[2], Dingena Schott and Jovana Jovanova

Faculty of Mechanical Engineering, Delft University of Technology, Delft 2628 CD, The Netherlands
[1] Current address: School of Mechanical Engineering, Southwest Jiaotong University, Chengdu, People's Republic of China.
[2] Current address: Information Hub, The Hong Kong University of Science and Technology (Guangzhou), Guangzhou, People's Republic of China.
* Author to whom any correspondence should be addressed.

E-mail: cqyaaron@gmail.com

OPEN ACCESS

RECEIVED
7 August 2025

REVISED
1 December 2025

ACCEPTED FOR PUBLICATION
9 December 2025

PUBLISHED
22 January 2026

Keywords: programmable morphing structure, robotic structure, shape memory alloy, shape memory polymers, modeling

Supplementary material for this article is available online

Abstract

Soft robotics requires structural systems capable of performing complex and programmable deformations to adapt to unstructured or dynamic environments. Shape memory materials (SMMs) offer a promising solution owing to their shape memory effect and stimulus-responsive adaptability. However, actuators relying on a single type of SMM are often constrained by nonlinear actuation behavior and limited stiffness variation, which restrict their ability to achieve coordinated, multifunctional responses. Addressing these challenges, this study introduces a hybrid programmable morphing structure that integrates a shape memory polymer (SMP) and a shape memory alloy (SMA) to realize cooperative actuation and adaptive stiffness variation within a single unit. In the proposed configuration, the SMA springs act as thermally activated actuators that generate deformation. The SMP cylindrical core employs its shape memory effect to realize reversible shape locking and serves as a thermal switch that enables controlled stiffness variation through temperature regulation. A coupled numerical model was established to describe the cooperative behavior between the SMA and SMP components, and the numerical results were validated through experimental testing. The agreement between simulations and experiments confirms the feasibility and repeatability of the proposed design. The structure achieves a maximum bending angle of 55° under dual-SMA actuation and 42° under single-SMA actuation, while maintaining any intermediate shape during thermal cycling. Furthermore, the hybrid system demonstrates a reversible six-fold increase in stiffness and a motion range extending up to three times its original length, representing a significant improvement over conventional single-material soft actuator. Moreover, the proposed hybrid structure offers a flexible strategy for programmable morphing and demonstrates scalable applicability in practical applications, such as adaptive grasping, reconfigurable locomotion, and environmental exploration. In conclusion, this work provides a feasible and generalizable framework for integrating multiple SMM into programmable morphing structures which can be applied into multifunctional soft robotic systems.

1. Introduction

Soft robotics, a multidisciplinary engineering field, has emerged from the need for flexibility and adaptability to perform tasks in unstructured environments [1, 2]. However, soft robotic systems still face several key challenges, including balancing compliance with stiffness, achieving multiple functions within a single structure, and adapting to dynamically changing environments [3, 4]. Incorporating smart materials into programmable morphing structures presents a promising way to overcome these challenges, as these systems can respond to external stimuli by utilizing their material behavior, structural configuration, and overall shape [5]. Thus, using programmable structures allows robotic systems to adjust their

shape and stiffness on their own autonomously in response to environmental changes. This ability results from the interaction between smart materials and structural design, rather than relying on complex control systems [6, 7]. To achieve this, the integration of smart materials and complex geometric design is important for programmable structures. While smart materials serve as actuators, complex geometries form the foundation of programmable morphing behavior, enabling functional transformations and adaptive responses.

As a type of smart material, shape memory materials (SMMs) are notable for their ability to remember and return to a predefined shape after undergoing significant deformation when exposed to specific external stimuli [8], when exposed to specific external stimuli. This unique property, observed in materials such Nickel–Titanium (Ni–Ti) alloy and polylactic acid (PLA), has broad applications in industries including aerospace, automotive, and precision manufacturing [9]. Theoretically, SMMs are categorized into two primary types: shape memory alloys (SMAs) and shape memory polymers (SMPs) [10]. SMAs are commonly used as soft actuators due to their relatively simple implementation. For example, a bionic jellyfish robot was developed to produce a contraction–recovery motion using an SMA [11]. In addition, Kakubari *et al* utilized strip-shaped SMA to control two silicone pillows, developing an artificial sphincter based on this setup [12]. Yang and Wang introduced a flexible gripper design with multiple finger units powered by SMA wires and a shorter rod [13]. Var and Jovanova developed a bioinspired flexible gripper actuated by SMA, designed for underwater environments as an add-on tool for maintenance and inspection tasks on autonomous underwater vehicles [14]. Sreesha *et al* experimentally developed an SMA-based bending actuator using 4D printing technology and evaluated its performance by printing actuators with different SMA compositions [15]. Based on this work, Ladakhan *et al* further demonstrated the cooperative actuation of multiple SMA wires, achieving faster response and significantly enhanced actuation force [16]. However, employing SMA alone as the actuation mechanism makes it difficult to achieve multiple deformation modes, and the structure is unable to provide variable stiffness, which is crucial for practical applications.

SMPs have become widely used due to their low density and high biocompatibility. Lan *et al* created a thermoset styrene-based SMP composite to construct a hinge mechanism for deploying a solar panel [17]. Son *et al* designed an adhesive gripper with a bonding strength greater than two atmospheric pressures, using the reversible dry adhesion of an SMP-based actuator [18]. Liu *et al* introduced a micro soft robot with four limbs, showing promise for medical applications, which was made with multiple layers of SMPs [19]. In addition, Risso *et al* proposed a novel design strategy that combines multi-stable structures with SMP. By exploiting both one-way and two-way shape memory effects, the structure is capable of shape programming, load-bearing, and self-actuation functionalities [20]. However, SMP actuators can only undergo passive shape changes, which limits their use as primary actuators in adaptive soft robotic systems. Moreover, Kim *et al* developed a hybrid composite actuator combining SMA and SMP, designed for morphing flaps with shape retention capabilities [21]. However, integrating SMA and SMP into a single actuator inevitably introduces structural constraints, which restrict the actuator to a single deformation mode and reduce its overall deformability. In addition, achieving effective coordination between actuation and stiffness regulation within such an integrated structure is still difficult to realize.

Morphing structures are designed to change shape in a reversible way, allowing robotic structures to perform different functions [22]. Morphing structures are designed to change shape in a reversible way, allowing robotic structure to perform different functions. In addition, unlike rigid systems with discrete movements, morphing structures deform continuously, enhancing energy efficiency and versatility [22]. SMMs enable programmable morphing structures capable of autonomously responding to environmental stimuli [23]. Specifically, the incorporation of SMAs into composite systems enables the realization of intelligent morphing structures with controllable shape deformation, delivering high recoverable strain and controlled shape recovery [24]. Furthermore, SMPs, through the integration of geometric configuration and microstructural design, facilitate reversible transformations within morphing structures, thereby establishing an effective linkage between form and function [25]. With these capabilities, morphing structures have been widely explored in various engineering domains, where their adaptive and reconfigurable nature enables diverse functional implementations [26, 27]. For instance, shape-morphing solar shading systems dynamically adjust to solar radiation and temperature, enhancing energy efficiency while reducing reliance on artificial lighting and cooling. Inspired by plant movements, they optimize light and heat control with minimal energy input, offering a sustainable, low-maintenance alternative to mechanical shading [28]. Robotic grippers benefit from shape morphing by using flexure hinges with morphable flaps to dynamically adjust stiffness. Inspired by origami, pneumatically actuated pouches control finger flexibility, allowing secure grasps of varied objects without complex control

systems [29]. However, morphing structures are usually driven by external actuators with fixed deforming modes [25]. Therefore, designing programmable structures requires a carefully coordinated integration of material properties and structural design, enabling multifunctionality while reducing dependence on external actuation systems.

To integrate programmable structures into soft robotic systems, this study presents a novel morphing structure that combines an SMP-based meta-structure with SMA-based springs. This design enables the coordinated actuation of multiple smart materials, facilitating programming deformation behaviors and enhanced adaptability. The primary contributions of this work are as follows. First, a hybrid morphing structure integrating both SMP and SMA is designed and evaluated through numerical simulations and experimental studies. Allowing for programmable and tailored deformation responses. This design provides a higher degree of freedom compared with existing hybrid structures that typically achieve only uniaxial or planar motions. Furthermore, the shared thermal driving system for both SMA and SMP materials enables alternate heating and cooling, allowing the structure to stop and restart instantly. Unlike previous designs that can only lock at the maximum deformation, our structure can lock and sustain any intermediate shape and then resume motion from that state. Besides, programmable structures are fully developed to comprehensively evaluate and optimize the programming deforming performance and adaptive stiffness, enabling their effective integration into robotic systems as functional components. Based on the functionalities, potential application scenarios in industrial engineering are explored, highlighting the practical value and scalability of the proposed programmable morphing structure.

2. Design of the programmable morphing structure

To achieve adaptable deformation in soft robotics, a programmable morphing structure comprising SMA springs and an SMP meta-structure is proposed as a single integrated unit constrained between two polymethyl methacrylate (PMMA) plates. The SMA components are made of Ni–Ti alloy, while PLA is used for the SMP material. As shown in figure 1(a), the design consists of an SMP core that is surrounded by three SMA springs. The SMA springs act as thermally activated actuators that contract upon heating and recover their original length during cooling, providing the driving force for structural deformation [30]. The SMP core functions as a thermal switch, modulating its stiffness to enable reversible shape locking. Once the desired deformation is achieved, the SMP transitions from a flexible to a rigid state as the temperature decreases, thereby locking the structure in the temporary configuration [31]. The cylindrical design of the SMP allows deformation and motion in multiple directions. During the recovery phase, the shape memory effect of the SMP plays a key role: the SMA springs first return to their pre-actuated elongated state, releasing the driving force, and then the SMP is reheated above its glass transition temperature to restore its initial shape. This cooperative mechanism between the SMA and SMP completes a closed actuation–fixation–recovery cycle, enabling both motion and self-recovery within the same structure.

The detailed geometric parameters of the structure are shown in figure 1(b). The SMP cylinder has a length (L) of 200 mm, an inner diameter (d_c), a wall thickness (t_p), and a height (u_h). The thickness of connection boards on both ends is t_c with a total diameter (D) of 106 mm. The deployment holes for the SMA springs are uniformly distributed along a circle with a radius (r_h) of 45 mm. The SMP meta-structure is defined by a wavy lattice unit. Each lattice unit has a total length (l_m) and a middle-gap length (l_h). The upper layer of the lattice has a thickness (t_u), while the lower layer has a thickness (t_d).

The working process of the proposed structure is illustrated schematically in figure 1(c). At room temperature (298 K), the structure initially remains straight. To begin actuation, the SMP component is first heated to reduce its stiffness, making it flexible enough to deform. Then, by selectively activating the three SMA springs through localized heating, the structure bends in controlled directions and at specific angles. Once the required shape is achieved, the SMP is cooled to regain its stiffness, thereby locking the structure into its new configuration. The bending performance is quantified using the bending angle (φ). When the SMA springs cool back to room temperature, reheating the SMP allows the structure to recover its original shape.

In addition to single-step transformations, the structure also supports stepwise transitions between configurations. As shown in figure 1(c), after reaching working configuration 1 and locking into place, individual SMA springs can be activated to further transform the structure into working configuration 2. This step-by-step mechanism allows the morphing structure to switch between multiple shapes, enabling a wide range of deformation modes for enhanced adaptive functionality.

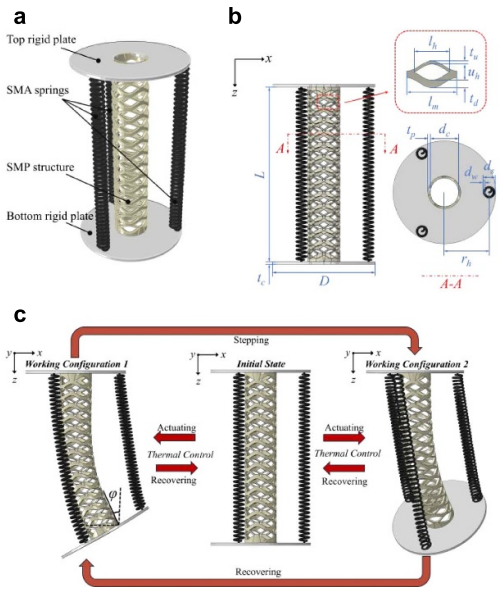

Figure 1. The proposed programmable structure and working principle. (a) Demonstration of the structure (b) geometric parameters (c) working process of the programmable structure.

3. Methodology

3.1. Numerical modeling

The finite element method is used in this study to model SMA and SMP, and analyze the performance of proposed morphing structure [32].

To simulate SMA behavior, an isotropic thermo-mechanical constitutive model was implemented in ABAQUS solver [33, 34]. The Helmholtz free energy per unit reference volume is calculated as shown in (1)–(4),

$$\psi = \psi^{\mathrm{e}} + \psi^{\xi} + \psi^{\tau} \tag{1}$$

$$\psi^{\mathrm{e}} = \widehat{\psi^{\mathrm{e}}}(\boldsymbol{E}^{\mathrm{e}}, \tau) = \frac{1}{2}\boldsymbol{E}^{\mathrm{e}}.C[\boldsymbol{E}^{\mathrm{e}}] - A(\tau - \tau_0).C[\boldsymbol{E}^{\mathrm{e}}] \tag{2}$$

$$\psi^{\xi} = \widehat{\psi^{\xi}}(\tau, \xi) = \frac{\lambda_T}{\tau_{\mathrm{T}}}(\tau - \tau_0)\xi \tag{3}$$

$$\psi^{\tau} = \widehat{\psi^{\tau}}(\tau). \tag{4}$$

In these expressions, ψ^{e} represents the thermo-elastic free energy density, $\boldsymbol{E}^{\mathrm{e}} = 1/2(\mathbf{C}^{\mathrm{e}} - \mathbf{I})$ is the elastic strain, and $\mathbf{C}^{\mathrm{e}} = \mathbf{F}^{\mathrm{e}T}\mathbf{F}^{\mathrm{e}}$ where is the elastic distortion. $\boldsymbol{A} = \alpha\mathbf{I}$ is the second order thermal expansion tensor where α being the thermal expansion coefficient. τ is the current temperature, and τ_0 represents the reference temperature. ψ^{ξ} represents the phase transformation free energy density, λ_{T} denotes the constant latent heat of phase transformation, $\xi \in [0, 1]$ is the martensitic volume fraction and $\tau_{\mathrm{T}} = (M_{\mathrm{s}} + A_{\mathrm{s}})/2$ is the transformation temperature where M_{s} is the martensite start temperature and A_s is the austenite start temperature. ψ^{τ} represents the pure thermal free energy density.

According to the Helmholtz free energy, the stress tensor can be expressed as shown in equation (5),

$$\boldsymbol{T} = \frac{\partial\psi}{\partial\boldsymbol{E}^{\mathrm{e}}} = C[\boldsymbol{E}^{\mathrm{e}} - \boldsymbol{A}(\tau - \tau_0)] \tag{5}$$

and the elastic distortion can be considered as part of the total deformation gradient $\mathbf{F} = \mathbf{F}^{\mathrm{e}}\mathbf{F}^{\mathrm{inel}}$, in which $\mathbf{F}^{\mathrm{inel}}$ denotes the inelastic transformation distortion obtained from equation (6),

$$\dot{\boldsymbol{F}}^{\mathrm{inel}} = \left\{\sqrt{1.5}\overline{\varepsilon_t}\dot{\xi}\,\boldsymbol{S}\right\}\boldsymbol{F}^{\mathrm{inel}} \tag{6}$$

where $\boldsymbol{S} = \frac{\mathrm{sym}(C^{\mathrm{e}}T)_{\mathrm{dev}}}{\left|\mathrm{sym}(C^{\mathrm{e}}T)_{\mathrm{dev}}\right|}$ is the inelastic flow direction and $\overline{\varepsilon_t}$ is the maximum transformation strain, which is 0.05.

In this study, Ni–Ti alloy wires (commercially is Flexinol) are with martensite start temperature $M_s = 325\,\mathrm{K}$, martensite finish temperature $M_f = 315\,\mathrm{K}$, austenite start temperature $A_s = 341\,\mathrm{K}$, and austenite finish temperature $A_f = 351\,\mathrm{K}$, were extracted from differential scanning calorimetry data provided by the material manufacturer and further confirmed through preliminary thermos mechanical characterization [35]. To ensure the stable transformation during the heating and cooling cycle, the operational temperatures in both simulation and experiment were selected as 298 K for cooling and 360 K for heating. This temperature range guarantees complete martensitic and austenitic transformation and maximizes the recoverable strain and actuation efficiency of the SMA springs. In addition, the elastic modulus of the alloy in martensite phase and in austenite phase are 28 GPa and 75 GPa, respectively.

To elucidate the mechanical behavior of SMP, the superimposed generalized Maxwell model and Williams–Landel–Ferry (WLF) equation within Abaqus finite element solver are utilized [36]. The corresponding constitutive relations for the multi-branch viscoelastic model are presented in equations (7)–(10),

$$\sigma(t) = \varepsilon_0 E_n + \varepsilon_0 \sum_{i=1}^{n-1} E_i e^{\frac{-t}{\tau_i}} \tag{7}$$

where $\sigma(t)$ represents stress at time t, ε_0 is the strain at the initial time, E_n represents the equilibrium modulus when the element is fully relaxed, E_i is the elastic modulus and τ_i is the relaxation time of the Maxwell element i. The relation of relaxation modulus E in the generalized Maxwell equation with time t is expressed in equation (8),

$$E(t) = E_n + \sum_{i=1}^{n-1} E_i e^{\frac{-t}{\tau_i}} \tag{8}$$

and the relaxation behavior satisfies the limiting condition described by equation (9),

$$\lim_{t\to\infty} E(t) = E_n \tag{9}$$

performing relaxation experiments at different temperatures and using the time–temperature equivalence principle is crucial. This approach enables the transformation of the relaxation response curves of SMP from various temperatures into a unified relaxation response curve at a chosen reference temperature. According to the WLF equation [36], the connection between the relaxation time at the present temperature T and the relaxation time at the reference temperature of T_r is expressed in equation (10),

$$lg\alpha_T = lg\frac{\tau}{\tau_r} = \frac{-C_1(T - T_r)}{C_2 + (T - T_r)} \tag{10}$$

where α_T represents shift factor, C_1 and C_2 are material constant. It is assumed that the glass transition temperature T_g is equivalent to the T_r. Furthermore, PLA was selected as the SMP component, and its viscoelastic and thermal properties were defined as follows, $T_g = 330$ K, $C_1 = 6.14$, and $C_2 = 293$ K [37]. At a temperature of 298 K, the material's elastic modulus was 1000 MPa, but it decreased by 60% when reaching the transition temperature.

In the simulation setup, the SMP cylinder was modeled using 5567 continuum linear hexahedral elements with a hybrid formulation (C3D8H) in ABAQUS. Each SMA spring was represented by 226 linear beam elements (B31H), while the PMMA components were discretized with 180 linear hexahedral elements of the C3D8H type. A fully bonded (fixed) contact interaction was defined between the SMP core, SMA springs, and PMMA components to ensure rigid connections and structural integrity throughout the assembly. In addition, alternating thermal boundary conditions were applied to activate SMA and SMP, enabling cooperative actuation within the numerical framework. Initially, the temperature of the SMP segment was set to 345 K, allowing the material to enter its rubbery state and become sufficiently flexible for deformation. The temperature of the SMA spring was then raised to 360 K, which is higher than its austenitic finish temperature, leading to spring contraction induced by the shape memory effect. Subsequently, the SMP layer was cooled to 298 K, causing a transition to the glassy state and locking the structure in the deformed configuration. Simultaneously, the SMA spring's temperature was reduced to 298 K to terminate actuation and extend to its original length. Finally, reheating the SMP to 335 K, which is above T_g, enabled the structure to return to its initial shape through shape memory effect, completing the full actuation, shape locking, and recovery cycle.

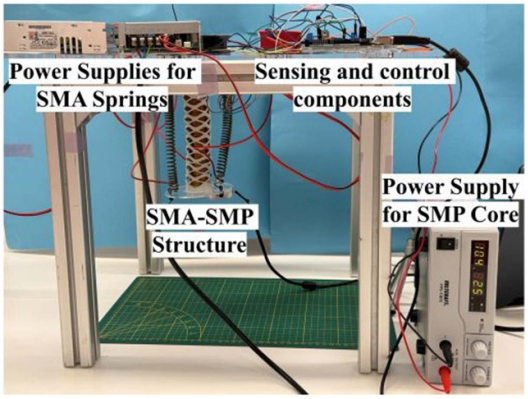

Figure 2. Experiments setup.

3.2. Experiment setup

The experimental setup is illustrated in figure 2. The SMP cylinder was fabricated using a Builder EXTREME 1500 PRO 3D printer and PLA filament. The SMA springs, made from a Ni–Ti alloy with a wire diameter of 2.3 mm, were selected for their stability and low risk of degradation. They were pre-trained to exhibit the two-way shape memory effect process [38]. The SMA springs are actuated through direct Joule heating, and no additional cooling system was required due to their relatively low cooling demand. Polyimide (PI) film heaters, custom-shaped to fit the inner surface of the SMP cylinder, were used to provide uniform heating assisted by a temperature sensing method. This design minimized interference with the structure's bending motion and ensured that the SMP is not exposed to external electrical inputs that could affect its performance. To improve thermal management and achieve reliable control of the SMP core, a fan was integrated at the top of the cylinder, while an air duct was installed to facilitate efficient heat dissipation and enable rapid temperature regulation of the SMP core. Combined with the sensing method, this configuration allowed precise control of the temperature distribution during the heating–cooling cycle of the SMP core. For accurate temperature measurement, an infrared thermal imaging sensor was positioned 50 mm from the cylinder along its central axis to avoid interference from the top and bottom ends. At each sampling point, the sensor captures a 32 $\times$ 24 temperature matrix, providing 768 temperature readings per frame. The sensing domain was divided into multiple regions to distinguish different thermal zones. The primary target region includes the area directly influenced by the exposed PI heater group and the outer surface shaped by cylinder thickness and heat transfer. Together these regions define the effective cross-sectional temperature range. The remaining regions account for thermal discrepancies introduced by geometric effects, radiative heat loss, and background conditions.

4. Results and discussion

4.1. Validation of the numerical modeling

To validate the feasibility of the proposed morphing structure, the bending performance was evaluated by comparing experimental results with numerical simulations. In this analysis, the fully loaded state refers to the maximum contraction achieved by a single activated SMA spring. The actuation process was quantified on a scale from 0 to 100, representing the percentage of the spring's contraction relative to its maximum capacity.

Figure 3 presents a comparative analysis, where figure 3(a) shows the results for the single-spring actuation mode, and figure 3(c) corresponds to the double-spring actuation mode. The root mean square error (RMSE) for single-spring actuation is shown in figure 3(b). In the single-spring scenario, the bending angle reached approximately 42° under full loading. The simulation results showed a near-linear trend, whereas the experimental values increased more gradually at the beginning, likely due to environmental influences or minor variations in material behavior. To quantitatively evaluate the deviation between the experimental and simulated results, the RMSE was calculated as a performance metric. The RMSE between experiments and simulations for single-spring actuation is shown in figure 3(b). The RMSE first increases and then decreases as the loading approaches its maximum, and the calculated value of 3.6° corresponds to 8% of the maximum bending angle, indicating good agreement between the simulated and experimental results. The error between the experimental and simulated results arises

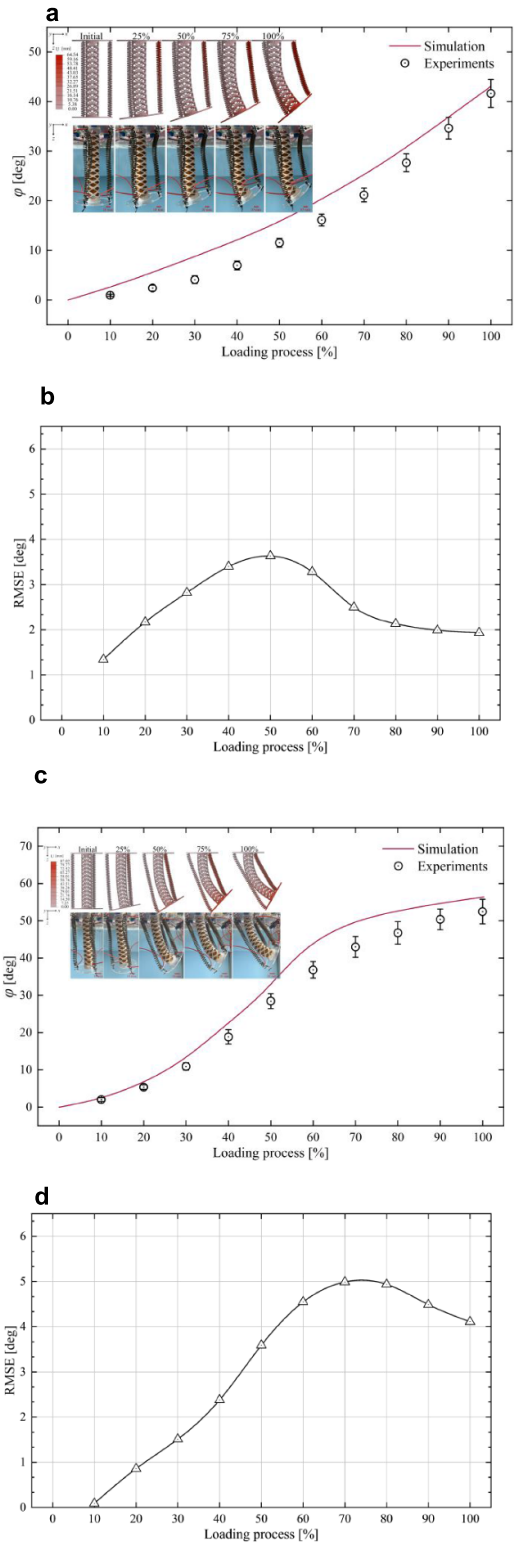

Figure 3. Validation of the bending performance. (a) Bending performances of the single-spring actuation (b) the RMSE between experiments and simulations of single-spring actuation (c) bending performances of the double-spring actuation (d) the RMSE between experiments and simulations of double-spring actuation.

mainly because the rigid joints in the experimental setup slightly restricted the bending of the structure. However, as the load approached 100%, the spring generated sufficient force to overcome these limitations, narrowing the gap between simulation and experiment.

For the double-spring actuation mode shown in figure 3(c), the structure achieved a higher maximum bending angle of around 55°, confirming that multiple actuators can enhance the deformation range. In contrast to the single-spring setup, the bending angle in the double-spring mode increased

steadily up to about 70% loading. After that, the bending rate slowed down because the SMP structure approached its maximum stretch, limiting further deformation between 70% and 100%. The RMSE between the experimental and simulated results for the double-spring actuation is shown in figure 3(d). Similarly, the RMSE initially increased and then decreased, yielding a final value of approximately 5°, corresponding to about 10% of the maximum bending angle. Despite the relatively higher RMSE, the simulation accurately reproduced the overall deformation trend and saturation behavior, confirming the reliability of the proposed model. The remaining discrepancy arose primarily from differences between idealized simulation conditions and real experimental environments. Friction and boundary constraints likely introduced additional resistance not represented in the model, while nonlinear material behavior and thermal lag in the SMA and SMP caused nonuniform temperature distributions and corresponding performance variations. These results confirm the feasibility and repeatability of the proposed morphing structure and highlight the advantages of integrating multiple SMA springs to achieve enhanced deformation capability.

4.2. Programming morphing performance of the structure

To systematically evaluate the programming morphing performance of the proposed structure, a sensitivity analysis was conducted by varying four key geometric parameters: wall thickness (t_p), lattice unit length (l_m), segment ratio ($r_s = t_u/t_d$), and structure height (u_h). These parameters were selected based on their critical roles in the deformation mechanics of the structure. All variations were constrained to ensure the SMP patterned lattice geometry remained structurally feasible and preserved the fundamental buckling-based deformation mechanism. To assess the stiffness, the bending stiffness (S_b) of the structure was defined as shown in equation (11) [22],

$$S_\mathrm{b} = \frac{F_\mathrm{b} L_\mathrm{b} \sin\beta}{\theta} \tag{11}$$

as shown in figure 4(a), F_b represents the external force applied at the free end, while L_b denotes the distance from the fixed end (top) to the point at which the force is applied. Therefore, the external bending moment about the fixed end is given by $F_\mathrm{b} L_\mathrm{b} \sin\beta$, where β is the angle between the direction of the applied force and the line connecting the fixed and free ends of the structure. In addition, θ denotes the rotational angle induced by the applied moment.

Figure 4(b) shows the bending performances affected by different influential parameters. First, a clear linear relationship happens between t_p and bending performance. As the t_p increases, φ decreases approximately linearly, while S_b gradually increases. Thicker wall enhances the overall structural rigidity but limits the achievable deformation range. Although increased thickness improves load-bearing capacity, it reduces the flexibility required for large morphing motions. Therefore, a balance must be achieved according to the specific application requirements: thinner cylinders are preferable when greater bending flexibility is needed, whereas thicker cylinders are beneficial when higher structural strength and load capacity are required.

The variation in l_m has a more significant influence on both φ and S_b. As l_m increases, φ rises rapidly up to approximately 30 mm, after which the growth becomes more gradual between 30 mm and 40 mm, resulting in an overall variation of about 50°. In contrast, S_b decreases with increasing l_m, showing an obvious drop when l_m exceeds 20 mm, with the total stiffness differing by nearly a factor of five across the examined range. To achieve an optimal balance between bending performance and structural strength, l_m should be selected within the range of 20–30 mm.

Similarly, variations in r_s show a trend comparable to that of t_p. As r_s increases, φ decreases while S_b increases gradually. The main difference is that both φ and S_b exhibit larger variation ranges. Specifically, φ differs by up to 30° across different r_s values, whereas S_b varies by nearly a factor of two. Therefore, in applications where a large load-bearing capacity is required and only moderate deformability is needed, r_s can be regarded as a main design parameter for performance optimization. Lastly, as u_h increases, φ rises, with a total variation of approximately 20°, while S_b decreases sharply, showing an overall reduction of nearly sevenfold. Therefore, in practical applications, a smaller u_h is preferable to maintain sufficient structural strength.

In summary, the sensitivity analysis reveals that different geometric parameters contribute differently to the deformation behavior and stiffness of the programmable morphing structure. Selecting appropriate parameter values is crucial to achieving an optimal balance between bending performance and structural strength, thereby ensuring suitability for a wide range of engineering applications.

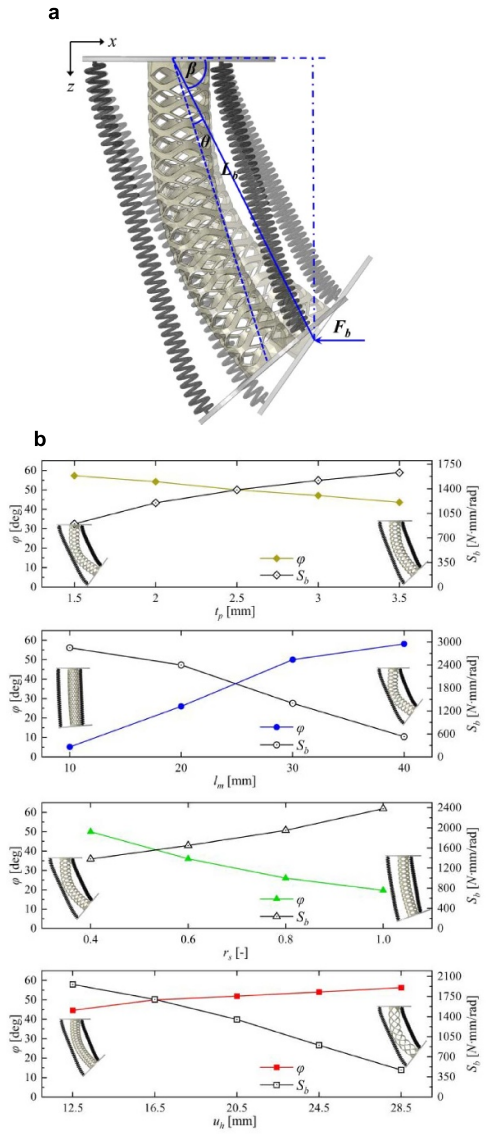

Figure 4. The bending performance analysis influenced by different parameters. (a) Illustration of the calculation of the S_b (b) bending performance plotted against four parameters.

4.3. Performance of the robotic structure

To further evaluate the feasibility of applying programmable morphing structures, this section presents a numerical analysis of their performance, focusing on structural flexibility, stiffness modulation capability, and adaptability to environmental variations. These characteristics are essential for their effective integration into soft robotic applications. The simulations were conducted under idealized conditions, in which a uniform temperature distribution was applied as a boundary condition and the effect of gravity was neglected, allowing the analysis to isolate the dominant thermo-mechanical deformation behavior and reflect conditions relevant to underwater applications.

The programmable morphing unit, composed of a single SMA-SMP hybrid structure, can be considered as a fundamental segment. These segments can be modularly combined with multi-segment systems capable of achieving more complex motion configurations. When multiple cylindrical modules are connected in series, each module can be independently actuated to bend in different directions, thereby enabling complex multi-axis deformation. To further investigate the motion capabilities of multi-segment configurations, we developed a dual-segment morphing structure in which two basic units were rigidly connected. In the structural design, each unit features two actuation modes, including single-spring and double-spring actuation, which are denoted as ‘s’ and ‘d’, respectively. Each unit can further bend either

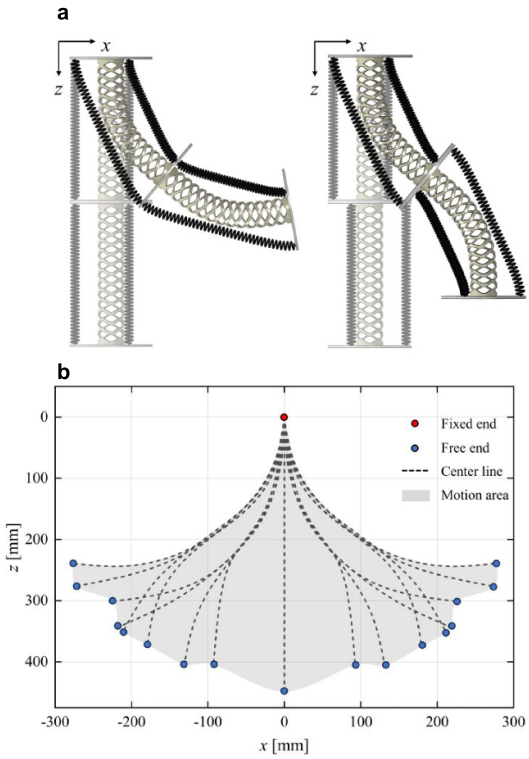

Figure 5. Double cylinder configuration. (a) Isometric view of the deformed state (b) displacement path of the deformed structure in the *YZ* plane.

in the positive or negative *x*-direction, indicated by '+' and '–'. By enumerating all possible combinations, a total of 16 bending mode configurations can be obtained. The resulting deformation characteristics and motion behaviors of the integrated structure were analyzed through numerical simulations.

For example, as shown in figure 5(a), the '+ d + d' configuration corresponds to both units undergoing double-spring actuation and bending toward the positive *x*-direction, resulting in an expanded overall range of motion. In contrast, the '+ d–d' configuration allows the two units to bend in opposite directions, enabling the structure to navigate deeper or more spatially constrained environments. This enhanced adaptability demonstrates the potential of dual-segment design for diverse application scenarios.

The displacements paths of all the bending configurations are illustrated in figure 5(b), the two-segment structure achieves a maximum extension nearly twice its original length during actuation. By varying the geometry of individual segments or selectively activating the SMA springs, the structure can be programmed to achieve diverse and tunable deformation behaviors, allowing the system to adapt to different tasks without altering its basic configuration. Moreover, additional segments can be attached to the free end, enabling modular and programmable designs that support tailored deformation configurations.

In summary, the modular design enhances both the flexibility and adaptability of the system and enables a high degree of motion programmability. This approach facilitates the integration of programmable morphing structures into soft robotic systems, enabling them to perform complex, task-specific deformations.

Stiffness variation is another critical factor for evaluating the feasibility of soft robotic systems in practical applications. In the proposed morphing structure, variable stiffness is achieved through the phase transition of the SMP core. To evaluate the S_b of the proposed structure, a constant external force was applied during simulations, and the resulting displacement response was used to calculate the stiffness under different thermal conditions. For consistency in comparison, the stiffness of the SMP core was evaluated at two characteristic temperatures, 335 K (rubbery state) and 298 K (glassy state), representing the soft and rigid phases, respectively.

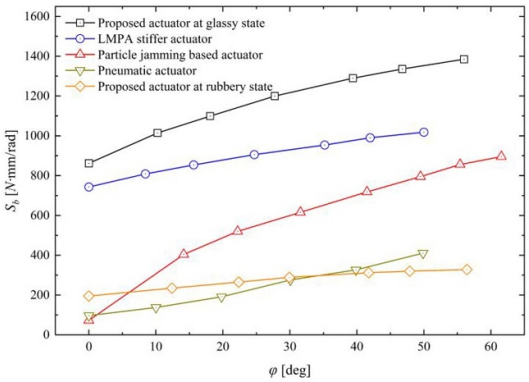

Figure 6. The S_b comparison of different actuators.

To evaluate the impact of stiffness variation in the proposed morphing structure, a comparative analysis was conducted against several actuators employing other stiffness variation methods, including a low melting point alloy (LMPA)-based actuator [39], a particle jamming based actuator [40], and a pneumatic actuator [41]. The results are shown in figure 6. The proposed morphing structure exhibited a significant increase in stiffness when the SMP core transitioned from the rubbery to glassy state, achieving a stiffness approximately six times greater. This result demonstrates the feasibility of utilizing the SMP phase transition for stiffness variation. Additionally, by balancing the SMP's phase transition with the flexibility of the embedded SMA springs, the structure can retain temporary shapes upon stiffness increase, effectively locking in specific configurations. This capability enables programmable deformation and enhances the adaptability of the morphing structure, thereby contributing to the realization of mechanical intelligence in soft robotic systems. Furthermore, the proposed morphing structure demonstrated superior stiffness performance compared with several widely used actuators. Specifically, it achieved stiffness values approximately 1.32 times higher than the LMPA-based actuator, 1.55 times higher than the particle jamming actuator, and maximum up to 7 times greater than the pneumatic actuator. These comparisons clearly highlight the structural advantages provided by the SMP-based core. Unlike other mechanisms that often rely on external equipment or complex material systems, the proposed design achieves reversible stiffness transition using only thermal activation. This not only simplifies system integration but also enhances reliability and energy efficiency. Moreover, local stiffness control can be achieved by the collaborative actuation of the SMA springs and SMP core, enabling multiple structural shapes under higher stiffness conditions.

By integrating both flexibility and tunable stiffness, the proposed programmable morphing structure demonstrated strong adaptability across a wide range of potential applications. As shown in figure 7, various potential configurations for practical applications were created by assembling multiple morphing units, and their responses under different actuation strategies were investigated through simulations. First, owing to its large deformation capability and tunable stiffness, the proposed morphing structure enables stable and conformal contact with target objects. As illustrated in figure 7(a), this feature allows a soft robotic arm constructed from the proposed structure to adapt its shape and effectively grasp large or irregularly shaped objects. Upon cooling, the stiffness of the structure increased, enhancing its load-bearing capacity and enabling a more stable and conformal grasping posture. Second, as illustrated in figure 7(b), when combined with programmable actuation, the morphing units can operate as robotic limbs for locomotion. Locomotion is achieved through a cyclic sequence of heating the SMP, activating the SMA, and subsequently cooling the SMP, ensuring stability during ground contact and flexibility during movement. Furthermore, as illustrated in figures 7(c) and (d), by programming the segments into different configurations, the proposed programmable robotic structures can effectively operate in unstructured or unpredictable environments, such as underwater pipeline inspections or narrow cave explorations in deep sea environment. After actuation, variations in structural stiffness allow the system either to lock its posture or to further adjust its configuration, providing the flexibility necessary for both stable operation and adaptive exploration tasks. Moreover, when combined with suitable sensing strategies, the system can achieve precise positioning, stable control, and reliable task execution. These

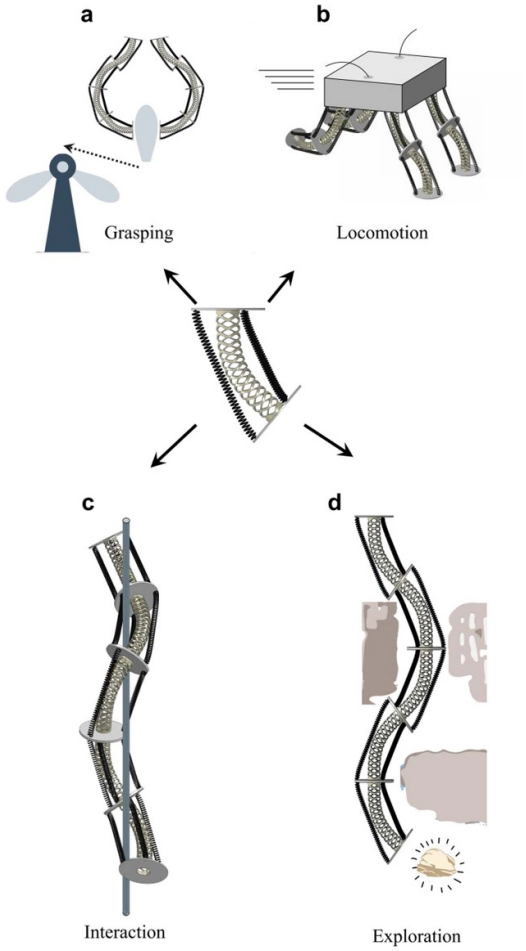

Figure 7. Different configurations of robotic structures. (a) Grasping irregular objects (b) locomotion (c) interaction in unpredictable environment (d) exploration in narrow cave.

results demonstrate the feasibility of the proposed structure as a programmable morphing system capable of multiple tasks. In addition, the proposed framework provides a conceptual foundation for developing practical prototypes and robotic systems in future engineering applications.

5. Conclusion

To embed programmable structures into soft robotic systems, this study introduces a novel morphing structure that integrates multiple SMMs to achieve distinct functions. The design combines a thermally responsive SMP meta-structure with SMA springs. This integration enables the structure to achieve large, programmable deformations and self-actuated motion. In addition, the coordinated interaction between the SMP core and SMA springs provides tunable stiffness, enabling the structure to lock into different configurations and adapt effectively to diverse working conditions.

The feasibility of the proposed design was validated through both simulations and experiments, which exhibited strong agreement. The structure demonstrated maximum bending angles of 42° under single-spring actuation and 55° under double-spring actuation. By adjusting the design parameters, the bending angle can be tuned over a wide range from 5° to 60°. Furthermore, stiffness variation through the SMP's phase transformation enabled the structure to increase its stiffness by up to sixfold. In its stiffer state, the proposed structure achieved stiffness values up to 1.55 times higher than those of comparably scaled stiffness-enhancing actuators. From a practical perspective, the modular design concept allows various configurations to be assembled, enhancing flexibility and adaptability. This provides strong potential for application in a wide range of soft robotic tasks, such as adaptive grasping, locomotion, environmental interaction, and exploratory operations.

In summary, the proposed programmable morphing structure presents a promising approach to embedding enhanced flexibility and adaptability into soft robotic systems through the integration of smart materials. Future research will aim to develop an integrated control and sensing framework that

improves motion precision and enables autonomous operation. In addition, the lattice geometry will be optimized using near-zero Poisson's ratio designs, such as chiral or re-entrant patterns, to achieve more uniform deformation and improved structural reliability.

Data availability statement

All data that support the findings of this study are included within the article (and any supplementary files).

Acknowledgment

This work is financially supported by Delft University of Technology and China Scholarship Council Grant No. 202006950011. In addition, thanks for the support from the IWS 3D printing workshop and experiments lab in the Faculty of Mechanical Engineering, Delft University of Technology.

Author contributions

Dingena Schott 0000-0001-5499-7123
Supervision (equal)

References

[1] Calisti M, Picardi G and Laschi C 2017 *J. R. Soc. Interface* **14** 20170101
[2] Tolley M T, Shepherd R F, Mosadegh B, Galloway K C, Wehner M, Karpelson M, Wood R J and Whitesides G M 2014 *Soft Robot.* **1** 213–23
[3] Fang J, Zhuang Y, Liu K, Chen Z, Liu Z, Kong T, Xu J and Qi C 2022 *Adv. Sci.* **9** 2104347
[4] Wang T, Jin T, Lin W, Lin Y, Liu H, Yue T, Tian Y, Li L, Zhang Q and Lee C 2024 *ACS Nano* **18** 9980–96
[5] Kortman V G, Mazzolai B, Sakes A and Jovanova J 2025 *Adv. Intell. Syst.* **7** 2400294
[6] Wang T, Pierce C, Kojouharov V, Chong B, Diaz K, Lu H and Goldman D I 2023 *Sci Robot.* **8** eadi2243
[7] Khaheshi A and Rajabi H 2022 *Adv. Sci.* **9** 2203783
[8] Casati R, Passaretti F and Tuissi A 2011 *Proc. Eng.* **10** 3423–8
[9] Bogue R 2009 *Assem. Autom.* **29** 214–9
[10] Sun L, Huang W M, Ding Z, Zhao Y, Wang C C, Purnawali H and Tang C 2012 *Mater. Des.* **33** 577–640
[11] Villanueva A, Smith C and Priya S 2011 *Bioinspir. Biomim.* **6** 036004
[12] Kakubari Y, Sato F, Matsuki H, Sato T, Luo Y, Takagi T, Yambe T and Nitta S-I 2003 *IEEE Trans. Magn.* **39** 3384–6
[13] Yang K and Wang Y 2008 *J. Mech. Sci. Technol.* **22** 895–904
[14] Var S C and Jovanova J 2023 *In Smart Materials, Adaptive Structures and Intelligent Systems* vol 87523 (American Society of Mechanical Engineers) pp V001T006A013
[15] Sreesha R B, Ladakhan S H, Mudakavi D and Adinarayanappa S M 2022 *Int. J. Adv. Manuf. Technol.* **122** 4421–36
[16] Ladakhan S H, Sreesha R B and Adinarayanappa S M 2024 *Prog. Addit. Manuf.* **9** 85–105
[17] Lan X, Liu Y, Lv H, Wang X, Leng J and Du S 2009 *Smart Mater. Struct.* **18** 024002
[18] Son C, Jeong S, Lee S, Ferreira P M and Kim S 2023 *Robotics* **12** 59
[19] Liu Z *et al* 2020 *IEEE Robot. Autom. Lett.* **5** 3291–8
[20] Risso G, Kudisch M, Ermanni P and Daraio C 2024 *Adv. Sci.* **11** 2308903
[21] Kim N-G, Han M-W, Iakovleva A, Park H-B, Chu W-S and Ahn S-H 2020 *Compos. Struct.* **243** 112227
[22] Chen Q, Schott D and Jovanova J 2024 *Sci. Rep.* **14** 26148
[23] Ji J, Zhang K and Guo X 2024 *Smart Mater. Struct.* **33** 085027
[24] Rodinò S and Maletta C 2024 *Prog. Eng. Sci.* **1** 100021
[25] Hwang D, Barron I I I E J, Haque A T and Bartlett M D 2022 *Sci Robot.* **7** eabg2171
[26] Dudek K K, Kadic M, Coulais C and Bertoldi K 2025 *Nat. Rev. Mater.* **10** 1–16
[27] Chafik A A, Gaber J, Tayane S, Ennaji M, Bourgeois J and Ghazawi T E 2024 *ACM Comput. Surv.* **56** 1–26
[28] Li Y, Zhao Y, Chi Y, Hong Y and Yin J 2021 *Mater. Today Energy* **22** 100874
[29] Godaba H, Sajad A, Patel N, Althoefer K and Zhang K 2020 *2020 IEEE/RSJ Int. Conf. on Intelligent Robots and Systems (IROS)* (IEEE) pp 8716–21
[30] Wang Z, Zu X, Feng X, Zhu S, Bao J and Wang L 2004 *Mater. Des.* **25** 699–703
[31] Behl M, Razzaq M Y and Lendlein A 2010 *Adv. Mater.* **22** 3388–410
[32] Sakhaei A H, Akbar S and Ge Q 2021 *14th WCCM-ECCOMAS Congress 2020* (unpublished)
[33] Sakhaei A H and Thamburaja P 2017 *Mech. Mater.* **109** 114–34
[34] Lagoudas D C, Bo Z and Qidwai M A 1996 *Mech. Compos. Mater. Struct.* **3** 153–79
[35] Lemke J and Coda A 2019 *Mater. Today Commun.* **21** 100666
[36] Ward I M and Sweeney J 2012 *Mechanical Properties of Solid Polymers* (Wiley)
[37] Wang J, Kean R, Randall J and Giles D 1998 *Int. J. Polym. Anal. Charact.* **4** 393–405
[38] Huang W and Toh W 2000 *J. Mater. Sci. Lett.* **19** 1549–50
[39] Chen Q, Schott D and Jovanova J 2024 *Soft Robot.* **11** 924–34
[40] Chen Q, Schott D and Jovanova J 2024 *J. Mech. Robot.* **16** 051004
[41] Jiang P, Yang Y, Chen M Z Q and Chen Y 2019 *Bioinspir. Biomim.* **14** 036009